Jovian Ammonia Cloud Identification and Color Analyses from Hyperspectral Imaging

Paul D. Strycker[1], N. J. Chanover[1], D. G. Voelz[1], A. A. Simon-Miller[2]

[1]New Mexico State University, [2]NASA Goddard Space Flight Center

Background: The two analyses presented here each involve long-standing puzzles of the Jovian atmosphere and use the same hyperspectral data set.

The first analysis concerns ammonia (NH_3) condensate clouds, which are inferred to be present on Jupiter (with a large coverage fraction) via thermochemical predictions. Thus far they have only been spectrally identified in the IR (1.99 μm and 2.74 μm) and persist over a short timescale (< 2 days) in small, localized regions of intense upwelling (Baines *et al.* 2002, Reuter *et al.* 2007). In our data, a strong absorption feature (>4σ) at 784 nm, a known NH_3 gas absorption band (Karkoschka 1998, Bowles *et al.* 2008), was seen in isolated areas of high cloud opacity and systematically differed from the locations of 644 nm NH_3 gas absorption features. This was the motivation for pursuing the questions: ***Can 784 nm absorption be used to trace NH_3 condensate? How similar are these regions to observations of spectrally identifiable ammonia clouds (SIACs)?***

The second analysis concerns the coloring agents (chromophores) in Jupiter's visible clouds. Previous analyses have been unable to conclusively identify which or how many chromophores are responsible for the color. Various analytical techniques, including principal components and cluster analyses, have been attempted previously, but have met with limited success due to low spatial or spectral resolution in the regions of interest (Dyudina *et al.* 2001, Simon-Miller *et al.* 2001a and 2001b, Thompson 1990, West *et al.* 1986). ***Hyperspectral image cubes are naturally suited to chromophore studies, and ours were acquired with this purpose in mind.***

Instrumentation: The unique hyperspectral data sets described below were acquired with the New Mexico State University Acousto-optic Imaging Camera (NAIC), which has the ability to acquire images with tuneable narrowband filtering (~15 Angstroms FWHM) between 0.4 and 1 micron using an **Acousto-Optic Tuneable Filter** (AOTF). Instant wavelength selection with the AOTF makes it possible to create spectral image cubes with better spectral resolution and coverage than feasible with standard narrowband filters, and the imaging camera provides better spatial resolution than possible with a spectrograph. Filtering with the AOTF requires passing light through standing acoustic waves in a TeO_2 crystal. The internal acoustic vibrations are induced by sending a radio frequency (RF) signal from an RF generator into the crystal via a transducer. The frequency of the RF signal determines the wavelength tuning of the filter.

Observations: Narrowband visible and near-infrared images of ~85% of Jovian longitudes were acquired at the Apache Point Observatory 3.5-meter telescope from 26-27 June and 04 July 2007 with NAIC. Exposure times were 2 seconds, and the seeing ranged from ~0.7-2.0 arcsec. Over 3000 images were collected, reduced, corrected for limb effects, and map-projected, yielding image cubes that span 480-900 nm with 2 nm resolution (**Figure 1**). Only ~65% of Jovian longitudes were mapped **(Future Work)**. The conditions were not photometric, so all analyses are based on the brightness contrast within each image.

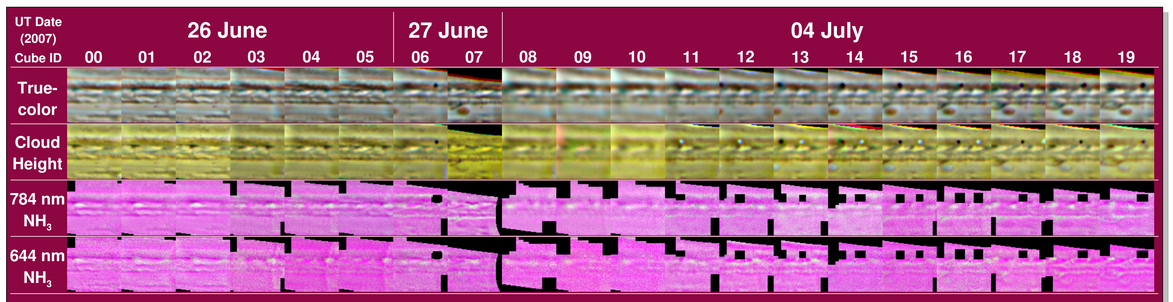

Figure 1: Map projections of Jupiter observations acquired with the Apache Point Observatory 3.5m telescope and the New Mexico State University Acousto-optic Imaging Camera (NAIC). Each spectral image cube represented here consists of ~211 narrowband images spanning 480nm-900nm at 2nm intervals. The latitudinal coverage in all cubes is 40°N-40°S (planetographic), the longitudinal range is ±40° from the sub-earth longitude at the central cube time, and the pixel scale is 1° in both axes. **True-color** (480nm ≤ blue < 500nm ≤ green < 580nm ≤ red < 800nm): Many high-opacity clouds are visible in the northern equatorial region. The GRS appears in cubes 06, 07, 12-19. The western edge of Oval BA is visible in the lower-right corner of cube 00. Io and/or its shadow (to the west) are found at ~15°N in cubes 06, 11-19. The poor image quality in cubes 08-10 is due to high airmass. **Cloud Height** (red=756nm, green=726nm, blue=888nm): Dark areas are relatively cloud-free, red clouds are deep, white clouds are high and thick, and blue clouds are high hazes (Simon-Miller *et al.* 2001b). **784 nm NH_3** (red=800nm, green=800nm/784nm, blue=756nm): White areas have high continuum/absorption ratios for the 784nm absorption band of NH_3. The highest 800nm/784nm ratios are found in the northern equatorial region (near cloud clearings) and northwest of the GRS. **644 nm NH_3** (red=660nm, green=660nm/644nm, blue=756nm): White areas have high continuum/absorption ratios for the 644nm absorption band of NH_3.

Ammonia Clouds

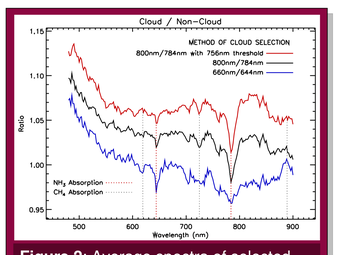

Figure 2: Average spectra of selected locations divided by the average spectra at the non-selected locations.

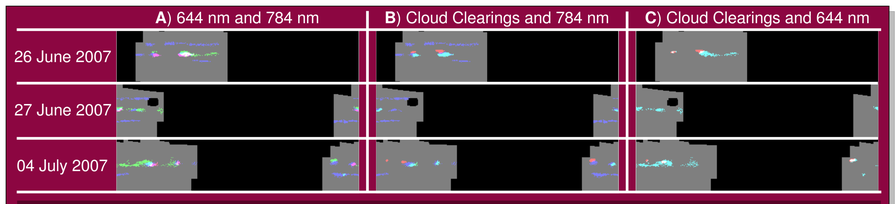

Figure 3: Maps of spectrally selected regions according to UT date. Each pixel is 1° in both axes (359° – 0° System III longitude from left to right and 40°N – 40°S planetographic latitude from top to bottom). Black denotes masked areas and longitudes with no observations. **Map A** (red=784nm and 756nm thresholds, green=644nm, blue=784nm): Although there is some overlap (white) between the 784 nm and 644 nm selections, the two absorption bands predominantly trace separate features. **Map B** (red=cloud clearings, green=784nm and 756nm thresholds, blue=784nm): For both 784 nm selection criteria, none of the regions overlap with the cloud clearings. **Map C** (red=cloud clearings, green=blue=644nm): Every cloud clearing is partially coincident (white) with 644 nm selections.

Ammonia Analysis: Regions in Jupiter's atmosphere with strong NH_3 absorption were determined by producing maps of the ratio between a continuum wavelength nearby an NH_3 absorption band and the band itself (**Figure 1**), resulting in larger ratios for a stronger NH_3 signal. The 644 nm and 784 nm bands were the only NH_3 absorption features with enough signal to noise to warrant study within the spectral range of the data. Three different criteria were then used to find "clouds" (referring here to adjacent loci, *not* the presence of condensates). Each cloud must have at least one point >4σ above the mean continuum/absorption ratio and extends to all adjacent points that are above the half-maximum ratio, as per Baines *et al.* (2002). An additional criteria, that the 756 nm continuum be >1σ above the mean at all points (no half-max extension), was used to further constrain the 784 nm clouds to locations with high opacity. Relatively cloud-free areas, "cloud clearings," are defined in the same manner as above, where the selection criterion is that $(756\text{ nm} \times 726\text{ nm})^{-1}$ be >4σ above the mean. These are considered a proxy for 5μm hot spots, and only those in the northern equatorial region were kept.

Figure 2 plots the ratio of the average cloud spectrum versus non-cloud spectrum for each selection method. The areas selected by the 784 nm absorption band with a 756 nm threshold (**red**) are brighter than average at all observed wavelengths and display the largest contrast between the 784 nm and 644 nm bands. Removing the 756 nm threshold yields locations with a ratio spectrum (**black**) darker by a few percent but very similar in spectral shape. 644 nm clouds (**blue**) are darker than average red-ward of ~600 nm. All three spectra show a strong negative slope from 480 nm to 550 nm.

Figure 3 displays the cloud locations as well as cloud clearings. The 784 nm clouds that include the 756 nm threshold will all be coincident with the other 784 nm clouds. Although there is some overlap between the 784 nm and 644 nm selections (white areas in **A**), the two absorption bands predominantly trace separate features. Even without the 756 nm threshold, the 784 nm clouds never overlap with the cloud clearings (**B**). However, every cloud clearing is partially coincident with 644 nm selections (white areas in **C**). The spatial characteristics of the 784 nm clouds constrained by the 756 nm threshold and the cloud clearings may be found in **Table 1** along with those of the SIACs and 5μm hot spots observed by Baines *et al.* (2002).

Ammonia Conclusions: Without a reference spectrum (at the relevant wavelengths) of NH_3 ice at Jovian temperatures and pressures, it is difficult to determine the physical nature of the 784 nm clouds. **This analysis cannot rule out the possibility that 784 nm absorption is entirely due to NH_3 gas, but 784 nm clouds clearly differ in size, location, and spectral shape from 644 nm clouds, indicating a different mechanism of production.** The 784 nm clouds have a component of 644 nm absorption in their spectra, however the 644 nm clouds do not have (comparatively) as strong of a 784 nm absorption feature. The 644 nm clouds are somewhat larger and seen in areas of lower cloud opacity (darker in 756 nm continuum and 726 nm CH_4 absorption, such as the identified cloud clearings), perhaps seeing down to lower altitudes (Cloud Height in **Figure 1**), which increases the likelihood that 644 nm clouds trace NH_3 gas as opposed to ice. A rigorous cloud-height analysis of the cloud regions in question would certainly shed more light on the issue.

Comparing 784 nm clouds with SIACs does highlight some major similarities but yields no conclusions. They have consistent global coverage fractions, although it is evident that the individual 784 nm clouds observed are very much larger on average (**Table 1**). Almost all of the 784 nm clouds are found in the 0°-5°N bin (**Figure 4**). This is quite comparable to SIACs, which are mostly found in the 2.5°-7.5°N (planetocentric) bin (Baines *et al.* 2002). Another similarity is their proximity in latitude to cloud clearings (5μm hot spots for SIACs) (**Figure 5**). The lifetime of the 784 nm clouds is on the order of days, as can be seen by the transience and gross alteration of features between observations (**Figure 3**, see also **Future Work**). SIACs have lifetimes approximately <2 days (Baines *et al.* 2002), which is probably due to rapid masking of the NH_3 ice spectral signature (Kalogerakis *et al.* 2008). A slower spectral masking rate at 784 nm (if there is any NH_3 ice absorption here) could account for the greater cloud sizes.

Table 1	Latitudinal Position (planetographic)	Latitudinal Size	Longitudinal Size	Observed Coverage	Global Coverage
784 nm Clouds (this work)	2.40°N ± 0.98°	4.89° ± 0.91°	11.19° ± 5.31°	0.92%	0.57%
SIACs (Baines *et al.* 2002)	6.47°N ± 0.53°	2.74° ± 0.77°	2.78° ± 1.56°	<1%	
Cloud Clearings (this work)	7.28°N ± 1.11°	3.05° ± 0.94°	6.78° ± 2.57°		
5μm Hot Spots (Baines *et al.* 2002)	8.07°N ± 0.35°	2.87° ± 1.28°	5.38° ± 2.44°		

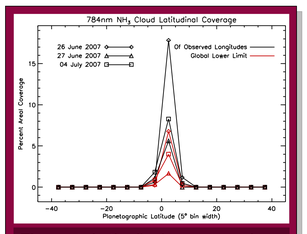

Figure 4: Latitudinal coverage of 784 nm NH_3 clouds (using the 756 nm threshold and computed in units of physical area) on three separate nights. **Black** denotes the percent coverage of the observed area, while **red** shows the lower limit of the percent global coverage (360° of longitude within each 5° latitude bin) by assuming that all unobserved longitudes have no 784 nm clouds.

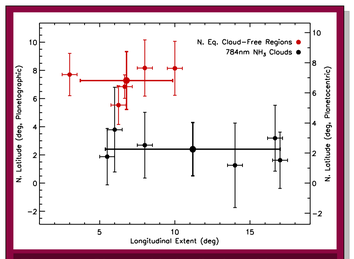

Figure 5: Size and latitudinal position characteristics of the 784 nm NH_3 clouds (**black**) and the northern equatorial cloud clearings (**red**). The mean and standard deviation of each population is in bold. Note that the abscissa is a longitudinal extent while the ordinate is a latitudinal location. The latitudinal extent of the cloud is gleaned from the size of the vertical bars.

Chromophores

Principal Components Analysis: A principal components analysis (PCA) finds an **orthonormal set of basis vectors that best describes the variance in the data**. Each principal component (PC) is a unit vector in the direction of the greatest variance remaining in the data after the removal of all contributions from previously determined PCs. PC1 is determined first, therefore it describes the largest contribution to the variance, and the rest follow in order of decreasing variance. **In color analyses, the PCs are in the form of spectra; however, they should not be interpreted as *physical* contributions to Jovian reflectance spectra.** Each PC may consist of positive and negative eigenvalue coefficients (negative contributions to reflectance spectra are unphysical), and the orthogonality constraint imposes itself on the spectral shape on every PC except PC1. An analysis which *does* result in describing physical components is nonnegative matrix factorization (NMF), which constrains all components to be nonnegative and does not impose orthogonality. An NMF analysis of the data presented here is currently in progress **(Future Work)**.

Table 2	NAIC Percent Variance	HST Percent Variance
PC1	77.27	94.43
PC2	8.60	4.10
PC3	4.33	0.88
PC4	1.93	0.32
PC5	0.99	

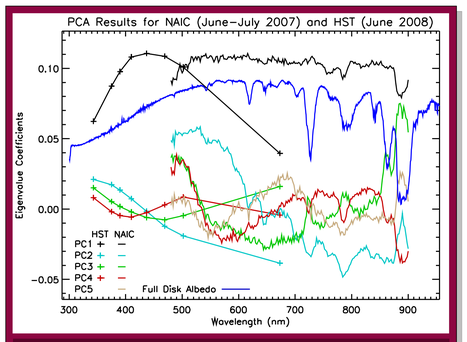

Figure 6: Principal components (PCs) from the HST and the NAIC principal component analyses (PCAs). The PCs are in order of descending variance, meaning that PC1 (**black**) describes the largest contribution to the variance in the spectral image cubes, followed by PC2 (**cyan**), etc. (see Table 2 for their variances). Jupiter's full-disk albedo spectrum (**blue**) is from Karkoschka (1998).

Principal Components Results: PCA was conducted on the NAIC image cubes as well as an HST/WFPC2 data set from 08 July 2008 immediately following the passage of Oval BA and the GRS (Simon-Miller *et al.* 53.02, this meeting) (**Table 2** and **Figures 6-8**). Simon-Miller *et al.* (53.02) found 4 significant PCs (before reaching the noise level) using 8 filters (**Figure 6**), and this work finds 5 significant PCs using 211 filters. The NAIC data are much noisier than the HST data, which is the reason that the non-noise PCs from NAIC only account for 93.12% of the total variance in the data versus 99.73% for HST. In both data sets the spectral shape of PC1 (**Figure 6**) describes the largest correlated deviations from the mean spectrum. From the maps of PC1 (**Figures 7** and **8**) it is seen that the highest positive values (green or white) are coincident with clouds that have high overall reflectivity (**Figure 1**) and vice versa. Although the subsequent PCs do not accurately represent the underlying spectral signatures (for reasons noted above), methane and ammonia absorption bands are clearly present (some are inverted). The additional PC from NAIC data not found in HST (not necessarily PC5 itself) is most likely due to our inclusion of methane absorption bands, which were absent from the HST analysis. **There are at least 5 statistically independent contributors to visible Jovian reflectance spectra.** These include methane and ammonia. There could be more than five for three reasons: (1) if two or more chromophores are spatially correlated, (2) if the wavelengths analyzed are insensitive to the spectral signatures of other chromophores, or (3) if their signals are below the noise level.

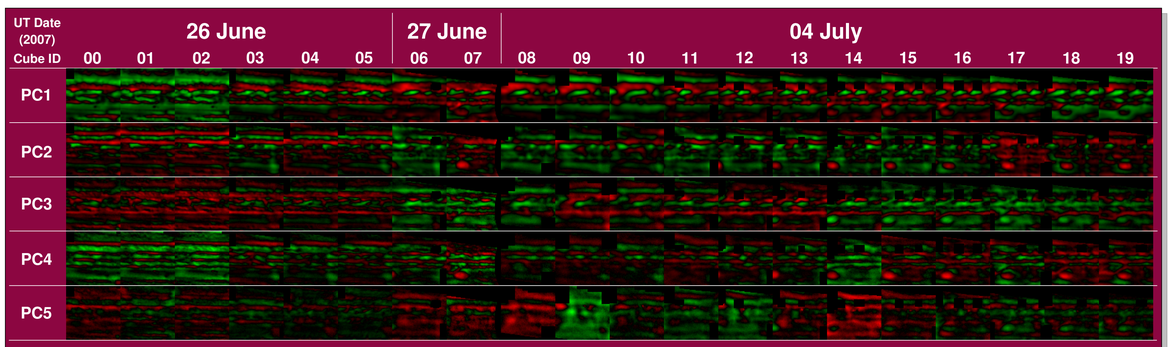

Figure 7: Maps of the first five PCs for the NAIC data. Green denotes positive values, and red denotes negative values. Note: The dynamic range has been independently stretched for each PC to aid viewing, thus brightness comparisons between different PCs are not meaningful.

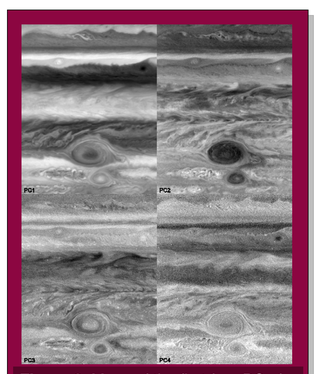

Figure 8: Maps of the first four PCs for the HST data. Black denotes negative values, and white denotes positive values. See note in Figure 7.

Future Work:

(**1**) The nonnegative matrix factorization analysis of this data will be completed.
(**2**) The data set described here will be remapped to include all important cloud features that are present (e.g. Oval BA).
(**3**) A spectral deconvolution will be performed on this data set, which should double the spectral resolution.
(**4**) Additional observations of Jupiter with NAIC will be proposed for its 2009 opposition to acquire more complete longitudinal and temporal coverage of NH_3 absorption bands.

References:

Baines *et al.* (2002) *Icarus* **159**, 74–94.
Bowles *et al.* (2008) *Icarus* **196**, 612–624.
Dyudina *et al.* (2001) *Icarus* **150**, 219-233.
Kalogerakis *et al.* (2008) *Icarus* **196**, 202–215.
Karkoschka (1998) *Icarus* **133,** 134–146.
Reuter *et al.* (2007) *Science* **318**, 223-225.
Simon-Miller *et al.* (2001a) *Icarus* **149**, 94-106.
Simon-Miller *et al.* (2001b) *Icarus* **154**, 459-474.
Thompson (1990) *Int. J. of High Performance Computer Applications* **4**, 48-65.
West *et al.* (1986) *Icarus* **65**, 161-217.

Acknowledgements:

The authors would like to thank Kevin Baines for helpful correspondences concerning his analysis of SIACs in *Galileo* NIMS observations.

This work is funded by the NSF (award number AST0628919).